

Navier-Stokes CFD Analysis of a Tidal Turbine Rotor in Steady and Planar Oscillatory Flow

G. Amato^{#1}, S. Doyle^{#2}, S. Petley^{#3}, M.S. Campobasso^{#4}, I.A. Milne^{*5}, G.A. Aggidis^{#6}

[#]Department of Engineering, Lancaster University, Gillow Avenue, LA1 4YW Lancaster, UK

¹giorgio.amato@stud.unifi.it, ²s.doyle1@lancaster.ac.uk, ³s.petley@lancaster.ac.uk, ⁴m.s.campobasso@lancaster.ac.uk,

⁶g.aggidis@lancaster.ac.uk

^{*}Centre for Offshore Foundation Systems, The University of Western Australia, 35 Stirling Highway, Crawley WA 6009, AU

⁵ian.milne@uwa.edu.au

Abstract—Initial results of an ongoing Navier-Stokes Computational Fluid Dynamics study of horizontal axis tidal current turbine hydrodynamics are presented. Part of the underlying motivation is assessing the effects of the Reynolds number on turbine performance and loads in steady and unsteady flow regimes. The study aims at a) providing initial verification and validation of Navier-Stokes CFD for steady and unsteady tidal turbine flows at tank experiment and field installation Reynolds numbers, and b) estimating the dependence of turbine performance and loads on this parameter to enable more reliable use of low-Reynolds number tank measurements for field installation analysis and design, and c) investigating crucial aspects of tank turbine hydrodynamics which are difficult to assess in the experiments. The investigation starts from a tidal current turbine towing tank experiment, compares available measured data and CFD results regarding the blade steady flow and unsteady flow due to the harmonic planar motion of the turbine, and then extends the CFD analysis to the high Reynolds numbers of typical utility-scale installations. It is found that at field-level Reynolds numbers, the blade power, force and moment coefficients are about 20 percent higher than at tank-level Reynolds numbers, and the agreement of measured and predicted loads at fairly low Reynolds numbers improves by modelling laminar-to-turbulent transition, highlighting the importance and extent of laminar flow phenomena and stall in tank experiments.

Keywords—Tidal turbine hydrodynamics, Reynolds number effects, wave loads, towing tank testing, Navier-Stokes Computational Fluid Dynamics.

I. INTRODUCTION

The UK and worldwide production of renewable electricity using tidal stream energy lags behind that of wind energy. Although power peaks of about 30 GW could be obtained by harnessing highly predictable UK tidal stream energy [1], the exploitation of this resource is still in its infancy and the installed tidal stream power capacity is well below these levels. Tidal energy exploitation with arrays of tidal current turbines (TCTs) is projected to grow in the next years, and this growth will require in-depth understanding of the complex interactions between TCTs and the marine environment, including their impact on sea bed characteristics, and marine fauna and flora.

The most rapidly growing utility-scale TCT type resembles that of multi-megawatt wind turbines: a 3-blade horizontal axis turbine with rotor speed and blade pitch power and load control. TCTs operate in harsh environments due to unsteady loads such

as those imparted by onset flow turbulence [2] and surface gravity waves [3,4]. Such unsteady loads may result in material fatigue, shortening the expected machine life, and thus compromising the financial success of the installation.

Flume and towing tank testing of reduced scale TCTs indicates that the peak-to-mean amplitude of the current turbulence-induced structural load can be more than 20 percent of the mean value [2]. Wave loads appear not to significantly alter the mean power and mean loads of TCTs [4,5], but they provide a substantial contribution to unsteady loads. Tank testing indicates that unsteady loads due to turbine inflow velocity fluctuations caused by surface gravity waves can be higher than turbulence-induced loads [3], with peak-to-mean load and power fluctuations comparable with their mean values. Moreover, large turbulent eddies can give rise to significant coherent unsteady loading on turbine blades even in absence of surface waves [6]. The complexity of the loads resulting from waves and coherent turbulent flow structures may be further aggravated by the occurrence of blade dynamic stall [7], triggered by the highest instantaneous water speeds during the wave cycle. The resulting hysteretic force cycles can significantly increase TCT fatigue loads. Furthermore, extreme wave-induced loads may occur due to faults of the speed/pitch/shut-down control systems.

TCT tank testing has played and continues to play a crucial role in improving the understanding of turbine steady hydrodynamics, unsteady hydrodynamics due to waves and turbulence, and also turbine wake characteristics [8,9], which are critical to understand and minimise energy losses in tidal arrays [10]; however, not all quantitative, and sometimes even qualitative tank testing data can be used directly for TCTs of field installations, because one cannot match all important non-dimensional numbers of field installations and reduced-scale experiments [11]. In reduced-scale TCT tank experiments, one uses ranges of tip-speed ratios (TSRs) λ similar to those of field installations to ensure the operating state of the rotor (*i.e.* inflow angles) is consistent. The TSR is given by:

$$\lambda = \frac{\omega R}{U} \quad (1)$$

where R denotes the rotor radius, ω its angular velocity and U is the free stream velocity. Two other crucial parameters which one would ideally maintain constant for scaled models and field installations are the Froude number $Fr = U/\sqrt{gh}$ and the

Reynolds number $Re = UD/\nu$, where g is the acceleration of gravity, h the water depth, ν the kinematic viscosity, and D the rotor diameter (in planned utility-scale arrays $D/h \approx 0.5$). Matching Fr is needed to model consistently the impact of waves and free surface proximity on TCT power and loads, and wake characteristics; matching Re is needed to model consistently the impact of both sea bed and rotor blade boundary layers on rotor performance. Due to their different dependence on h and D , it is impossible to match both Fr and Re . In most experiments, Fr matches that of field installations, but Re never does, and it often lies in a phenomenological range different from that of field installations, potentially yielding different hydrodynamic characteristics of field and lab TCTs. The Re mismatch and the λ match between field and model TCT give a mismatch of the Reynolds number Re_c based on the blade peripheral velocity and chord c at a given radius r , defined as:

$$Re_c = \frac{\omega r c}{\nu} \quad (2)$$

Unavoidably, the profile of Re_c along the blade of the model TCT for tank testing is between 1 and 2 orders of magnitude smaller than that of full-scale TCTs. The Re_c mismatch has two consequences: one is that the power, force and moment coefficients of model and real turbines may differ substantially, since such coefficients depend on lift and drag coefficients, which, in turn, can vary substantially with Re_c (at low Re_c lift coefficients are smaller, and large laminar separation bubbles often occur on the blade suction surface (SS) and, for thick foils, separation on the pressure surface can also occur), the other is that, in the presence of large velocity fluctuations, the Re_c mismatch may also result in misestimates of unsteady loads. A related example of the strong impact the Reynolds number may have on the performance and loads of renewable energy fluid machinery is reported in [12], which shows that the mean power coefficient of an oscillating wing for tidal power generation increases by about 18 percent as the Reynolds number increases from 1,100 to 1,500,000, due to notably different hydrodynamic phenomena at the two regimes.

Navier-Stokes (NS) Computational Fluid Dynamics (CFD) can be used to analyse turbine loads irrespective of the turbine size and operating conditions, and thus support both tank and field TCT development. CFD has a vast potential to support the development of utility-scale TCTs in light of the high costs and technical challenges of TCT field testing. It can also complement the knowledge obtainable with model TCT tank testing due to its potential of thoroughly assessing complex aspects of rotor hydrodynamics that are difficult or impractical to measure in experiments. TCT CFD, however, is a relatively new area, and it thus requires extensive verification and validation. Pioneering CFD studies of turbine-resolved NS CFD analyses of TCT hydrodynamics include the analysis of a TCT tank experiment in [13], and the multi-physics analysis of a field TCT in [14].

NS CFD can be used to assess the sensitivity of performance and steady and unsteady TCT loads to the Reynolds number, and thus enable designers to extrapolate with more confidence the findings of tank testing to field installations, quantitatively accounting for the aforementioned Re and Re_c mismatch.

This paper addresses these issues, and presents initial results obtained by analysing a recent TCT towing tank experiment [7] with the ANSYS® FLUENT® NS CFD code. In the experiment, power curves and steady loads are measured at different rotor and relative current speeds (corresponding to a relatively narrow range of the Reynolds number), and the unsteady loads acting at the blade root due to harmonic variations of the relative current velocity are also measured.

The main objectives of this work are to a) provide initial verification and validation of Navier-Stokes CFD for steady and unsteady TCT hydrodynamics, and b) estimate the dependence of TCT performance and loads on this parameter at both towing/flume tank scales and field scales. The study also investigates the impact of transition modelling on the analysis of flow regimes where transition is expected to play a key role.

Section II summarises the experimental set-up and the measurements that were reported by [7] and Section III describes the computational set-up of all CFD analyses. Section IV presents and discusses the steady and unsteady CFD analyses for selected operating conditions of the towing tank experiment, and Section V reports CFD analyses of an up-scaled TCT obtained from the model TCT of the experiment, but with operating conditions typical of field operation. The conclusions of this initial investigation are given in Section VI.

II. TOWING TANK MEASUREMENTS

The TCT experiments considered herein [7] were conducted at the Kelvin Hydrodynamic Laboratory of Strathclyde University in Glasgow. The towing tank has a working length of 76 m and a width of 4.6 m; the water level was maintained at 2.23 m in all experiments. The three-blade horizontal axis turbine employed in the experiments had a tip and hub diameter of 0.734 m and 0.120 m respectively. The blades were tapered and twisted (the radial profiles of chord and twist are reported in [7]), all blade sections conformed to the 24% thick NREL S814 profile [15], and the blade twist axis was at 30% chord from the leading edge. Figure 1 shows a photograph of the model turbine, and the dimensions of the tank cross section and the rotor swept area are provided in Fig. 2.

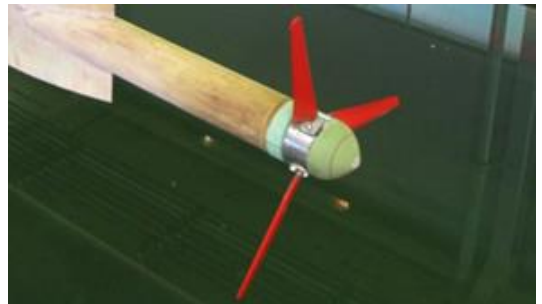


Fig. 1. TCT model [7].

Steady flow conditions were obtained while towing the turbine mounted on a carriage sliding on rails along the tank at a user-specified uniform speed and at different user-specified rotor angular speeds. The translational speed of the turbine would correspond to the free-stream tidal flow incident to the

turbine. Different TSRs could be obtained by varying either the carriage speed or the rotor angular speed.

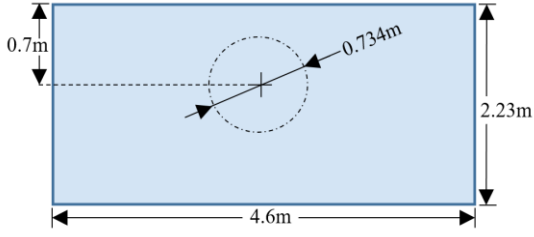


Fig. 2. Dimensions of towing tank cross section and rotor swept area.

Unsteady flow conditions associated with periodic variations of the oncoming water speed due to surface gravity waves or large coherent turbulent structures were modelled by superimposing a harmonic axial velocity component to the otherwise constant translational speed of the main carriage. The harmonic velocity component was achieved by mounting the turbine on a user-programmable secondary carriage fixed to the primary carriage. The combination of the translation motion of both carriages gives:

$$u(t) = U + \tilde{u} \sin(2\pi ft) \quad (3)$$

where U is the constant velocity of the main carriage, \tilde{u} is the peak velocity of the secondary carriage, and f denotes the frequency of its harmonic motion.

The rotor torque Q and axial thrust T were measured by a dynamometer mounted on the turbine shaft. Knowledge of torque and rotational speed enabled calculation of the turbine power P . Denoting the water density by ρ , and the area swept by the rotor by $A = \pi R^2$, the definitions of the thrust and power coefficients used in [7] and the present numerical study are provided by Eqs. (4) and (5) respectively:

$$C_T = \frac{T}{0.5 \rho U^2 A} \quad (4)$$

$$C_P = \frac{P}{0.5 \rho U^3 A} = \frac{Q\omega}{0.5 \rho U^3 A} \quad (5)$$

The blades were also instrumented with strain gauges at its cylindrical root at a radius of 36 mm from the rotor axis. The out-of-plane and the in-plane root bending moments were measured on separate blades. In both the experiments and the present CFD study, the out-of-plane blade root bending moment M_y is the moment of the blade hydrodynamic forces with respect to an axis normal to the rotational axis and at 36 mm from it; the in-plane blade root bending moment M_x is the moment of the blade hydrodynamic forces with respect to an axis parallel to the rotational axis and at 36 mm from it. The definition of the root bending moment is:

$$C_{M_i} = \frac{M_i}{0.5 \rho A U^2 R} \quad (6)$$

where the subscript i is y for the out-of-plane and x for the in-plane blade root bending moment.

Steady velocity tests were performed at constant rotor speeds between 63 and 96 RPM, and carriage speeds between 0.45 and 1.01 m/s. Reference [7] provides the time averaged power,

thrust, out-of-plane and in-plane blade root bending moments as a function of TSR. These coefficients exhibited a sensitivity to the rotational speed, most likely due to the variation of the Reynolds number Re_c with the rotational speed, and it was found that the maximum C_P for the considered range of rotational speeds varied in the interval $3 < \lambda < 4$.

The steady flow experiments of [7] provided the baseline against which the role of unsteadiness could be assessed by reconstructing quasi-steady response curves of the rotor for the instantaneous operating conditions of the unsteady tests, and comparing such quasi-steady response to the actual time-dependent response. In this numerical study the measured steady rotor characteristics at 73 and 96 RPM are instead used to perform preliminary verification and validation of various aspects of the considered CFD model (Section IV), and assess the impact of the Reynolds number variability on a wider range, covering the values of this parameter encountered in tank testing and field installations (Section V).

To characterise the unsteady flow experiments, [7] defines the current number μ as the ratio of the maximum oscillatory velocity to the mean current velocity ($\mu = \tilde{u} / U$), a parameter akin to the turbulence intensity. Realistic values of 0.1, 0.2 and 0.3 were analysed in [7], and the simulations reported in Sections IV and V use $\mu=0.2$ and frequency $f=0.5$ Hz. The two operating conditions of the experimental rig considered in Section IV are those associated with $\lambda=3.6$, $U=0.78$ m/s and rotational speed of 73 RPM, and $\lambda=4.1$, $U=0.89$ m/s and rotational speed of 96 RPM. The field-representative high-Reynolds number analysis of Section V uses instead only the operational condition at $\lambda=4.1$.

III. NUMERICAL SET-UP

All NS CFD analyses reported herein were performed using the commercial ANSYS® FLUENT® package. In both steady and time-dependent analyses, the CFD model comprised only one blade and gravity was not included in the simulation. This was deemed to be a suitable approach due to the lack of significant axial velocity variations in the steady flow experiments, and the small ratio of the vertical to horizontal scales of motion in oscillatory flow experiments [16]. The free surface was also not modelled both to simplify the set-up of these initial analyses, and because both the steady and oscillatory motion of the turbine induced relatively low levels of free-surface displacements and velocities in the considered experiments. Moreover, the blockage of the rotor based on the projected frontal area was 4.7% [7], which represents a relatively low value, and for this reason all simulations reported herein considered a circular cross section of the domain rather than the rectangular one of the actual towing tank. In light of the observations and approximations above, a 120° wedge-shaped domain was utilised. The physical domain is depicted in Fig. 3, which also indicates the boundary conditions adopted in the simulations.

The flow equations are solved in the rotating frame of reference but with respect to frozen absolute velocity components. The velocity imposed at the inlet and the

cylindrical far field boundaries is the axial speed of the turbine, whereas a constant static pressure is enforced at the outlet boundary. Flow periodicity is enforced on the lateral boundaries of the domain which enabled a reduction in computational costs by 1/3 with respect to the case of a full rotor analysis. Figure 3 reports all domain sizes as a function of the blade tip radius R .

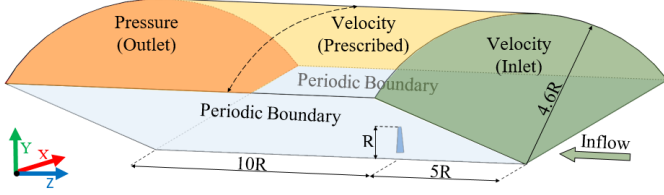


Fig. 3. Computational domain and boundary conditions.

For the turbulence closure, all CFD analyses used Menter's $k-\omega$ Shear Stress Transport (SST) model [17] with a low-Reynolds number correction similar to that of Wilcox's $k-\omega$ model [18]. In the CFD simulations which also model the laminar-to-turbulent transition, the one-equation γ model of Menter has been used [19] (these transitional analyses model turbulence and transition with three equations, two for the SST model and one for the γ model). The free stream turbulence intensity and ratio of turbulent and laminar viscosity have been set to 0.1% and 0.1 respectively.

All computational grids were generated using ANSYS® Meshing™ and they are of a hybrid type, consisting of a structured zone surrounding the blade and tetrahedral cells between the structured zone and the far field boundaries. Three grids have been used in this study: a coarse grid (CLR) and a fine grid (FLR) for the analysis of the towing tank experiment of Section IV, and a fine grid (FHR) for the high-Reynolds number analyses of Section V. Views of the blade surface mesh and the section with a planar slice at $0.75R$ of grid CLR are provided by the left and right images of Fig. 4 respectively.

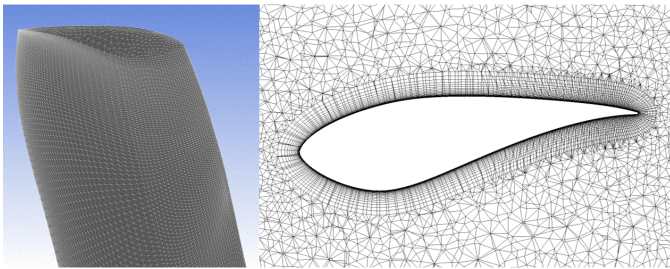


Fig. 4. Left: tip region of blade surface mesh (CLR). Right: grid past blade on plane slice at $0.75R$ (FLR).

Grids CLR, FLR and FHR contain about 4, 12 and 13 million elements respectively. Their main characteristics are reported in Tab. 1, in which $c_{75}=42$ mm is the hydrofoil chord at $0.75R$, δ is the minimum wall distance, H_i is the height of the structure grid zone around the blade, and N_h , N_R , N_i and N_{EL} denote respectively number of elements along each blade hydrofoil, number of elements along the blade length, number of inflation layers around the blade, and total number of grid elements.

TABLE I
SUMMARY OF THE MESH PARAMETERS

	CLR	FLR	FHR
δ/c_{75}	1.4e-04	5.9e-05	3.3e-06
H_i/c_{75}	0.13	0.07	0.08
N_h	130	220	250
N_R	125	275	250
N_i	18	30	30
N_{EL}	4.3e06	12.3e06	13.1e06

IV. TOWING TANK SIMULATIONS

A. Steady Analyses

The first set of experiments analysed with the numerical setup discussed in Section III are for steady flow past the model turbine at $\omega=73$ RPM for a range of main carriage speed corresponding to $2.81 < \lambda < 5.06$. The measured and computed power coefficient C_p , thrust coefficient C_T , out-of-plane root bending moment C_{My} , and in-plane root bending moment C_{Mx} are compared respectively in the top left, top right, bottom left and bottom right subplots of Fig. 5. The abbreviations 'CLR' and 'FLR' are defined in Section III; 'Turb' denotes fully turbulent simulation, and 'Trans' denotes transitional simulation.

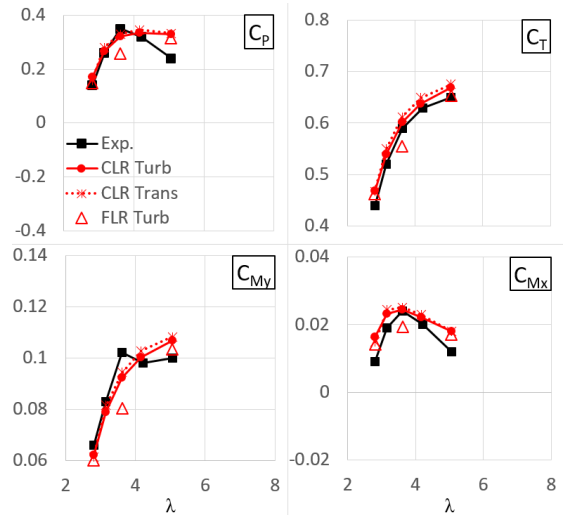


Fig. 5. Measured data [7] and CFD results for different TSRs at $\omega=73$ RPM ('CLR' and 'FLR' denote coarse and fine grid respectively, 'Turb' denotes fully turbulent simulation, and 'Trans' denotes transitional simulation). Top left: power coefficient; top right: thrust coefficient; bottom left: out-of-plane root bending moment; bottom right: in-plane root bending moment.

All CFD thrust estimates were obtained by adding to the axial force acting on the three blades the differential pressure force acting on a zero-thickness disk centred on the rotor axis and covering the rotor hub omitted in the CFD model. One notes that the prediction of all four coefficients using the fully turbulent and the transitional coarse grid analyses differ fairly little, and that the difference between the two predictions is marginally larger at higher λ . This is because for the low Reynolds numbers associated with this steady operating condition (the value of Re_c at $0.75R$ given by Eq. (2) is about

88,000) boundary layers undergo significant separation at low TSRs, as shown below; predicted separation patterns appear to be fairly insensitive to the boundary layer state at these low Reynolds numbers, and the use of a transition model has thus very little impact on blade loads. At higher TSRs, lower angle of attack (AoA) and higher Reynolds number along the blade reduce the amount of flow separation, and the main effect of modelling transition is to increase the percentage of laminar boundary layers on the blade, possibly slightly reducing viscous drag and increasing lift due to thinner boundary layers.

One also notices that the agreement of measured and coarse grid predictions of thrust and out-of-plane bending moment is fairly good over the λ range considered, whereas the agreement of measured and coarse grid power and in-plane root bending moment coefficients worsens as one moves from $\lambda=3.6$ to higher values. This trend is also visible in the CFD analyses of [20], which considered a TCT towing tank experiment very similar to that examined herein. One possible reason for such mismatch of CFD predictions and measurements at high TSR is the lack of free-surface modelling in these analyses. Larger free surface deformations occurring at higher TSR in the towing tank may have resulted in lower streamwise water speed ahead of the turbine yielding lower values of the angle of attack to the blades, and thus lower tangential forces than predicted by CFD simulations which neglect free surface dynamics, and thus overestimate lift coefficients and tangential forces due to water speed overestimates. Figure 5 reports the CFD results obtained with a fully turbulent simulation using the fine grid FLR. Unexpectedly, the fully turbulent CLR and FLR predictions differ significantly at $\lambda=3.6$, the TSR yielding maximum power coefficient, whereas they are fairly close at the minimum and maximum TSRs. This result is surprising also because a) the refinement of the coarse grid is already fairly high, b) this phenomenon does not occur when considering a higher rotor speed, as shown later, and c) the maximum and average values of the nondimensionalised minimum wall distance y^+ are well below 1 for both coarse and fine grids (for grid CLR the maximum y^+ around the blade and across all TSRs is 1.5 and the maximum average value across all TSRs is 0.4; the FLR grid counterparts are instead 0.55 and 0.15). The sudden power and load drop at $\lambda=3.6$ predicted by the fine grid is due to a substantially larger amount of separation on the blade SS with respect to the coarse grid prediction. This may be the result of multiple concurrent factors including significant boundary layer instability at this low Reynolds number, very low numerical dissipation due to the use of a highly refined grid, and destabilising effect of the very low free stream turbulence intensity (this study uses 0.1%, whereas the CFD simulations of [20] used a value of 5%, assumed on the basis of flow turbulence induced by vibrations of the main carriage).

The top left and top right plots of Fig. 6 depict the velocity vectors on a cylindrical sectional slice of the blade at 0.5R and 0.8R respectively for $\lambda=2.81$, while the bottom left and bottom right plots provide the same type of information for $\lambda=3.6$. Cross-comparison of these plots highlights that, as expected, a) the amount of separation on the blade SS is significantly higher at the minimum TSR, and b) for given TSR the magnitude of

flow separation decreases from the central part of the blade to the outboard region, due to decreasing AoA and downwash due to the tip vortex. The plots of Fig. 6 also provide the contour levels of the radial component of the fluid velocity, and highlight that, at the deep stall conditions associated with the minimum TSR, the peak radial velocity in the separated flow region at 0.5R is comparable with the far field relative velocity.

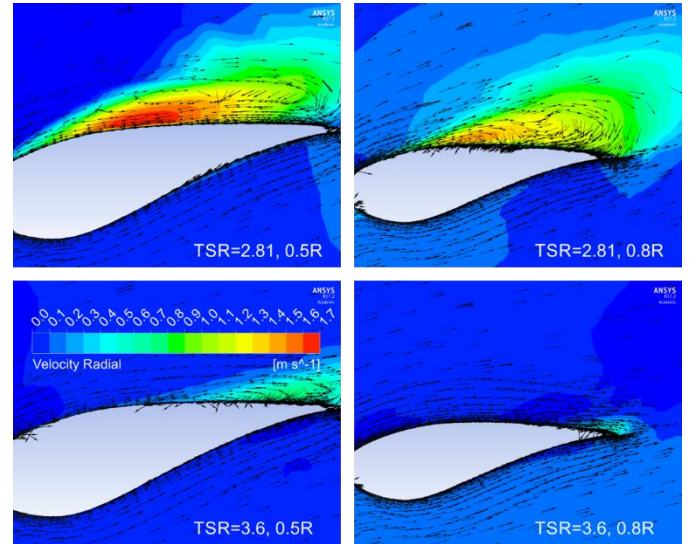


Fig. 6. Computed velocity vectors and contours of radial velocity components of towing tank TCT at $\omega=73$ RPM. Top left: cylindrical slice at 0.5R and $\lambda=2.81$. Top right: cylindrical slice at 0.8R and $\lambda=2.81$. Bottom left: cylindrical slice at 0.5R and $\lambda=3.6$. Bottom right: cylindrical slice at 0.8R and $\lambda=3.6$.

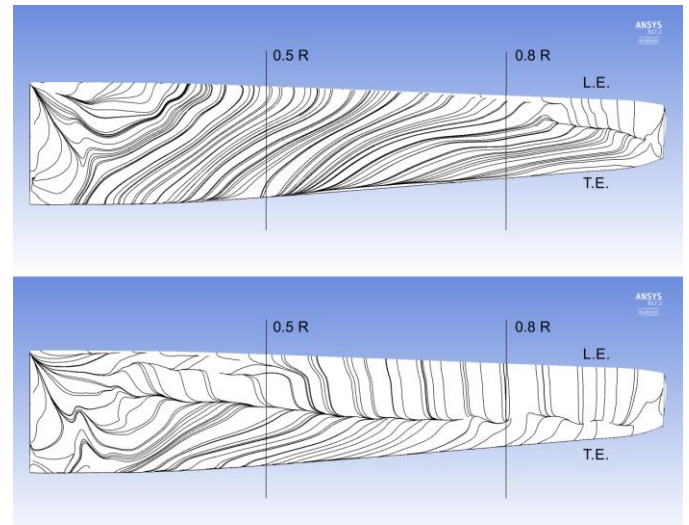


Fig. 7. Computed wall shear stress lines on the SS of the blade of the towing tank TCT at $\omega=73$ RPM at $\lambda=2.81$ (top plot) and $\lambda=3.6$ (bottom plot).

These phenomena are visualised in a more global fashion inspecting the wall shear stress lines on the blade SS of Fig. 7, in which the top plot refers to $\lambda=2.81$ and the bottom one to $\lambda=3.6$ (L.E. and T.E. denote respectively leading and trailing edge). The former plot highlights a large separation encompassing most of the blade SS, and confirms the existence of a significant radial component, as seen in Fig. 6. The bottom

plot of Fig. 7 shows that only about half of the blade upper side experiences flow reversal at $\lambda=3.6$, but the velocity vectors of the bottom plots of Fig. 6 highlight that the strength of such separation is substantially lower than at minimum TSR. The radial flow component at this low Reynolds number regime is due to the lower flow momentum at the lower radii, where the stream on the blade SS separates due to a) the existence of significant laminar boundary layer patches which have low resistance to adverse pressure gradients, and b) the high loading due to high AOA, only partly compensated for by the blade twist. The low momentum fluid in the stalled region is pushed outwards by the centrifugal force due to the blade rotation.

The nondimensionalised minimum wall distance y^+ was found to be of order 1 or less in all CFD analyses of the paper. As an example, the curves of averaged and maximum y^+ at the blade SS obtained with grids CLR and FLR for all considered TSRs at 73 RPM reported against λ in Fig. 8.

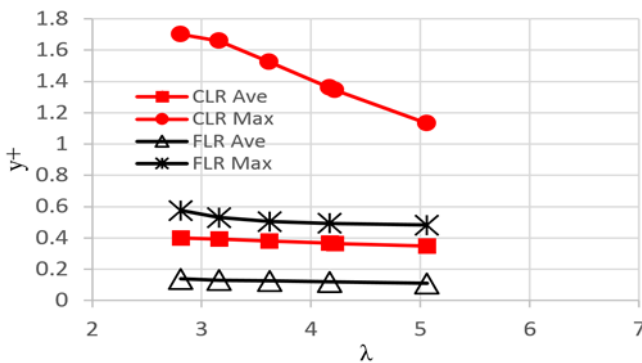


Fig. 8. Minimum and averaged y^+ on the SS of the blade of the towing tank TCT against TSR at $\omega=73$ RPM.

Figure 9 provides a comparison of the same type of that of Fig. 5, but for an angular speed of 96 RPM. The blade Reynolds numbers are thus higher than those considered in the preceding case, and the value of Re_c at $0.75R$ given by Eq. (2) is now about 116,000. The TSR range covered by the CFD analyses is $2.81 < \lambda < 6.61$, although the minimum TSR available from the measurements is 3.66. The overall trends emerging from the comparison of simulations and measurements is similar to that observed at 73 RPM. The agreement close to the peak power coefficient is reasonable, but progressively worsens as TSR increases. Unlike at 73 RPM, however, one now notes a larger difference of measured and computed out-of-plane root bending moment close to the peak power coefficient. The reasons for this are still unclear, and this occurrence is also in contrast with the very good agreement of the overall axial thrust in the same TSR interval. The omission of blockage and free surface modelling are presently unlikely to account for these discrepancies. Based on the frontal area of the rotor, the blockage was relatively low (less than 5 percent) compared to previous studies such as [21] (between 7 and 17 percent) and [22] (30 percent). The study of [21] found that the effect of blockage was to increase their measured thrust coefficient by 5 percent. Therefore, one would expect that the Strathclyde experiment, which had a 40 percent lower blockage, affected by a much smaller extent the measured data discussed herein.

Additionally, following the approach of [22], who provided a theoretical analysis of the free-surface effect for tidal turbines, the influence of the free surface in the Strathclyde tests is also expected to be sufficiently small. Ongoing CFD analysis will however verify these hypotheses.

As in the 73 RPM case, the difference between the fully turbulent and transitional coarse grid results is fairly small, but unlike in that case, the differences in the power and moment between the coarse and fine grid results are quite small for all considered TSRs, indicating that at this regime, the refinement of the coarse grid is sufficient to obtain a grid-independent result (for grid CLR the maximum y^+ around the blade and across all TSRs is 1.9 and the maximum average value across all TSRs is 0.5; the FLR grid counterparts are instead 0.68 and 0.17). This occurrence is most likely a consequence of the higher stability of blade boundary layers at 96 RPM due to overall higher Reynolds number.

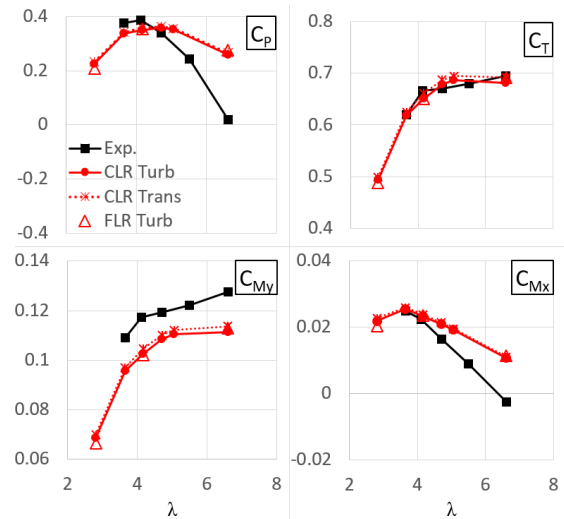


Fig. 9. Measured data [7] and CFD results for different tip-speed ratios at $\omega=96$ RPM ('CLR' and 'FLR' denote coarse and fine grid respectively, 'Turb' denotes fully turbulent simulation, and 'Trans' denotes transitional simulation). Top left: power coefficient; top right: thrust coefficient; bottom left: out-of-plane root bending moment; bottom right: in-plane root bending moment.

The top left and top right plots of Fig. 10 depict the velocity vectors and the contours of the radial velocity component on a cylindrical sectional slice of the blade at $0.5R$ and $0.8R$ respectively for $\lambda=2.81$, while the bottom left and bottom right plots provide the same type of information for $\lambda=4.1$, which yields maximum power coefficient at the 96 RPM condition. The qualitative trends are the same observed at lower angular speed (Fig. 6); however, the flow separation on the blade SS is now smaller, particularly at minimum TSR, where the ratio of peak radial velocity and far field relative velocity is significantly lower than at 73 RPM.

The lower level of stall is also confirmed by the wall shear stress lines of Fig. 11, in which the top plot refers to $\lambda=2.81$, and the bottom one refers to $\lambda=4.1$. Cross comparison of the results of Figures 7 and 11 reveals that for the highest loading conditions ($\lambda=2.81$), the flow on the SS is not entirely separated at 96 RPM (top plot of Fig. 11) unlike the 73 RPM case (top plot of Fig. 7). Similarly, the amount of separation at peak

power coefficient conditions is significantly smaller for the higher rotational speed case.

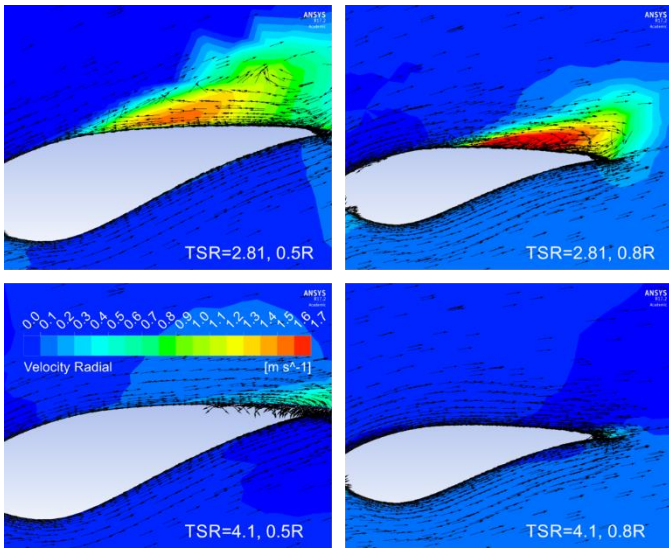


Fig. 10. Computed velocity vectors and contours of radial velocity components of towing tank TCT at $\omega=96$ RPM. Top left: cylindrical slice at $0.5R$ and $\lambda=2.81$. Top right: cylindrical slice at $0.8R$ and $\lambda=2.81$. Bottom left: cylindrical slice at $0.5R$ and $\lambda=4.1$. Bottom right: cylindrical slice at $0.8R$ and $\lambda=4.1$.

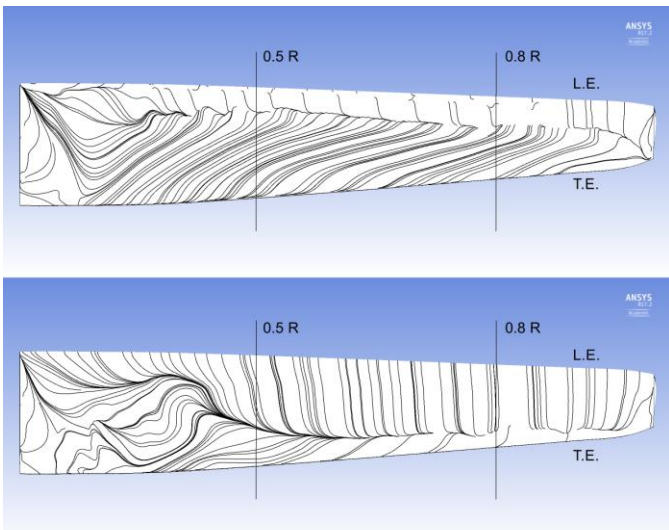


Fig. 11. Computed wall shear stress lines on the SS of the blade of the towing tank TCT at $\omega=96$ RPM at $\lambda=2.81$ (top plot) and $\lambda=4.1$ (bottom plot).

It is noted that a relatively small variation of the Reynolds number between the 73 and 96 RPM cases (about 30 percent) yields fairly large variations of flow patterns, rotor performance and loads (e.g. a measured peak power coefficient of 0.35 at 73 RPM and one of 0.39 at 96 RPM). This is due to larger extent of laminar boundary layers at 73 RPM, which makes adverse pressure gradient-induced separation more likely to occur.

The discussion above on stall levels cannot be backed up directly with experimental flow measurements, but the good agreement between measured and computed integral data at $\lambda=2.81$ (Figures 5 and 9) supports the correctness of the CFD analysis.

B. Unsteady Analyses

The first oscillatory flow condition considered herein is that associated with main carriage speed of 0.78 m/s, $\lambda=3.6$, current number $\mu=0.2$, and oscillatory frequency f of the secondary carriage of 0.5 Hz. The measured C_{My} is plotted against the instantaneous TSR in Fig. 12, along with CFD estimates obtained with grid CLR using a fully turbulent and a transitional analysis.

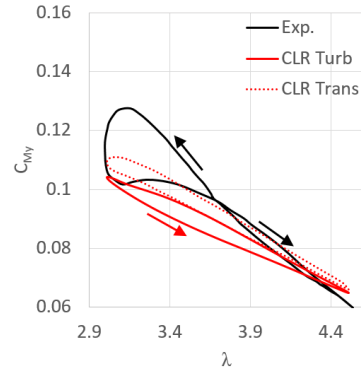


Fig. 12. Measured data [7] and CFD results for the time-dependent out-of-plane blade root bending moment against instantaneous TSR at $\omega=73$ RPM, mean $\lambda=3.6$, $\mu=0.2$ and $f=0.5$ Hz.

The overall agreement, particularly in terms of minimum and maximum moments is fairly good. The predicted hysteresis cycles at the lower TSRs are thinner than the measured one, indicating that the simulations predict less dynamic stall than observed in the measurements. This type of shortfall occurs frequently in RANS CFD using linear eddy viscosity models, and is often due to insufficient reliability of this approach in the presence of large flow separations. Significant improvements are expected by using anisotropic RANS turbulence models or hybrid RANS/LES CFD methods. One also notes that the prediction improvements achieved by using a transitional turbulence model are significantly higher than in steady flow conditions, as the transitional flow prediction improves further the agreement between the mean values of C_{My} at low TSRs. Improvements to the transition modelling set-up adopted herein (e.g. use of the two-equation $\gamma-Re_\theta$ transition model) may also result in improved agreement of measurements and simulations, due to improved prediction of the time-dependent separation point. Measured and computed moments are plotted against the oscillation period of the secondary carriage in Fig. 13, which further highlights the better agreement of transitional CFD and measurements. The transitional simulation gives a significantly better prediction of the time at which stall starts, when the maximum moment in the first quarter of the period occurs (this is well before the carriage velocity reaches its maximum); however, the predicted growth rate of the moment is smaller than in the experiment, and this results in a smaller moment drop with respect to that observed in the experiment. This is the reason for the thicker hysteresis loop for $\lambda<3.5$ visible in Fig. 12.

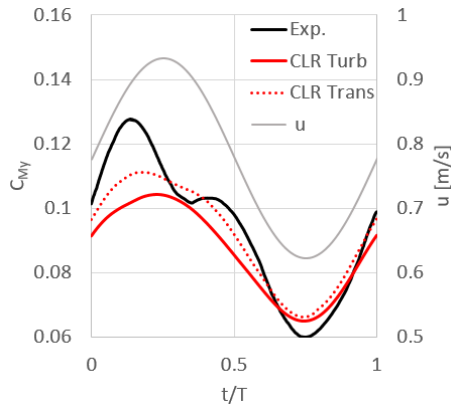


Fig. 13. Measured data [7] and CFD results for the time-dependent out-of-plane blade root bending moment over the oscillating cycle at $\omega=73$ RPM, mean $\lambda=3.6$, $\mu=0.2$ and $f=0.5$ Hz.

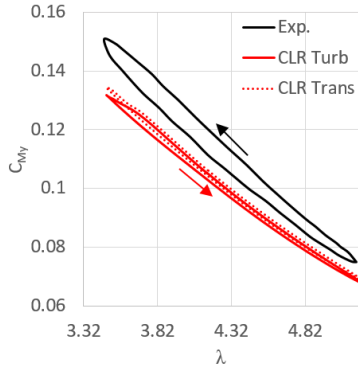


Fig. 14. Measured data [7] and CFD results for the time-dependent out-of-plane blade root bending moment against instantaneous TSR at $\omega=96$ RPM, mean $\lambda=4.1$, $\mu=0.2$ and $f=0.5$ Hz.

The second oscillatory flow condition analysed below is that associated with main carriage speed of 0.89 m/s, $\lambda=4.1$, current number $\mu=0.2$, and oscillatory frequency of 0.5 Hz. The measured C_{My} is plotted against the instantaneous TSR in Fig. 14, along with CFD estimates obtained with grid CLR using a fully turbulent and a transitional analysis. At this higher Reynolds number blade stall is less severe, and both measurements and simulations reveal a much more regular pattern of the moment loop than at 73 RPM. The qualitative agreement of experimental and CFD data has also improved with respect to the lower speed case, as the measured and computed amplitudes are in good agreement. Additionally, the differences between the fully turbulent and transitional results are significantly lower than at 73 RPM, which is probably due to more stable boundary layers at 96 RPM.

Preliminary analyses of the periodic solution sensitivity to the time-step were also carried out. It was found that the transitional solutions based on grid CLR and using 128 and 256 time-intervals per period differ negligibly (50 iterations were used in both cases), but the impact of increasing concurrently spatial and temporal refinement is still under investigation. All unsteady simulations were run for 10 oscillation periods to achieve a periodic state. The solution of the flow field at each time of the unsteady analyses (performing 50 iterations) using grid CLR and the 16 cores of one Intel(R) Xeon(R) E5-2650 v2 processor required about 1.9 or 2.6 minutes (wall-clock time)

depending on whether the fully turbulent or the transitional flow model was used.

V. HIGH-REYNOLDS NUMBER SIMULATION

A. Steady Analyses

To assess the dependence of performance and load characteristics on Reynolds number values typical of field installations, a set of operating conditions of a TCT with diameter of 20 meters is considered. The same blade geometry of the tank experiment is used. Other researchers have successfully used alterations of the scaled rotor blade geometry to match the thrust coefficient curve of the corresponding full-scale TCT [23] with the aim of matching the wake structure of model and full-scale TCT. This has not been done in this study because this method does not guarantee matching of the blade bending moment loads, whose assessment is one of the aims of this report, and also requires reductions of the foil thickness of the model blade, possibly introducing notable differences between the hydrodynamics of scaled and field rotors, due to the thicker foils of the latter ones. It is assumed that at $\lambda=4.1$ the tidal stream speed is 2.5 m/s. Using Eq. (2) to calculate Re_c at $0.75R$ and the scaled chord of 1.1 m at $0.75R$, one finds $Re_c=8.4$ million, which is about 70 times larger than in the towing tank experiment at the same TSR. The numerical set-up used for the CFD analyses of the up-scaled turbine is the same reported in Section III: the turbine dimensions are the same as those of the turbine in the tank but the fluid viscosity is scaled so as to achieve the Reynolds numbers of the field installation. The up-scaled turbine flow analyses use grid FHR, which differs from grid FLR due to a significantly smaller minimum wall distance required to ensure that y^+ is of order 1 or less on the blade surface at all operating conditions.

Figure 15 compares the fine grid fully turbulent predictions of power coefficient C_P , thrust coefficient C_T , out-of-plane root bending moment C_{My} , and in-plane root bending moment C_{Mx} . An expected qualitative outcome is that all high-Reynolds number curves are higher than their low-Reynolds counterparts. These results, however, highlight quantitatively the impact of the Reynolds number mismatch between tank and field TCTs. For example, at $\lambda=4.1$, the power coefficient and the out-of-plane root bending moment of the up-scaled turbine are about 23 and 18 percent higher than in the tank test. The percentage difference of C_T and C_{My} for the two scenarios increases from $\lambda=4.1$ to $\lambda=6.6$. The causes of this trend, due primarily to the difference of Reynolds number, are being investigated.

The left and right plots of Fig. 16 report the velocity vectors and the radial velocity component around the blade on cylindrical sectional slices at $0.5R$ and $0.8R$ respectively, and these results should be compared with their low-Reynolds counterparts in Fig. 10 ($\omega=96$ RPM). One notes that at field installation Re_c , the amount of separation at minimum TSR has decreased even further with respect to the $Re_c=116,000$ case, and that at close-to-maximum power, there is no more stall. This is confirmed by the wall shear stress lines of Fig. 17, which show that at the design TSR, the flow on the blade is predominantly two-dimensional and fully attached.

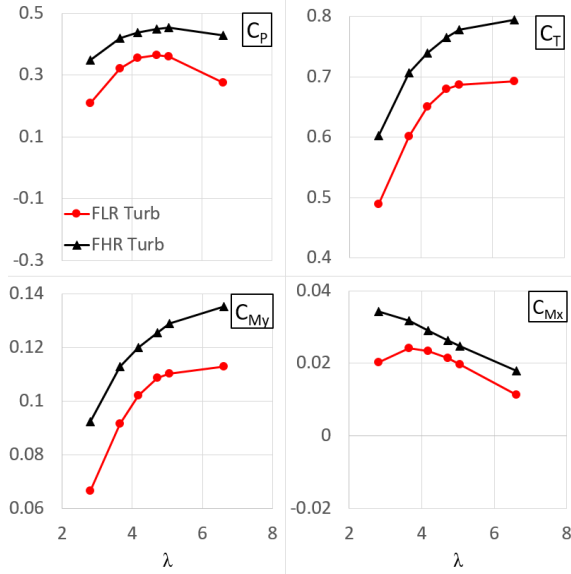


Fig. 15. Low- and high-Reynolds number CFD results for different TSRs at $\omega=96$ RPM ('FLR': fine grid for $Re_c=116,000$ analysis; 'FHR': fine grid for $Re_c=8.4$ million analysis. 'Turb': fully turbulent analysis). Top left: power coefficient; top right: thrust coefficient; bottom left: out-of-plane root bending moment; bottom right: in-plane root bending moment.

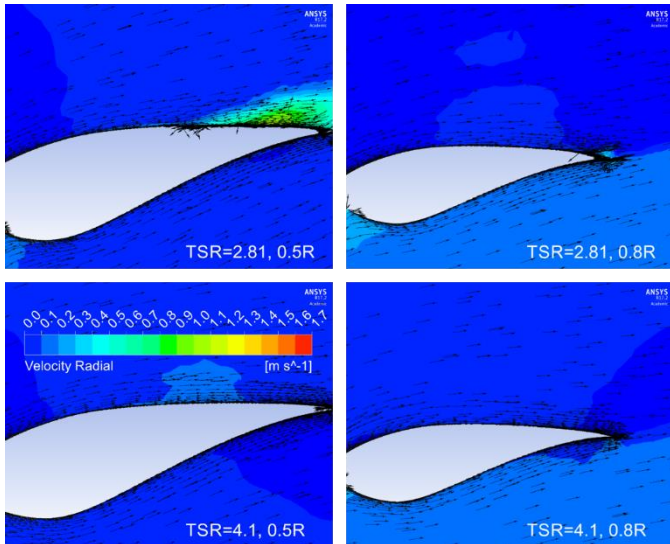


Fig. 16. Computed velocity vectors and contours of radial velocity components at $\omega=96$ RPM and $Re_c=8.4$ million. Top left: cylindrical slice at $0.5R$ and $\lambda=2.81$. Top right: cylindrical slice at $0.8R$ and $\lambda=2.81$. Bottom left: cylindrical slice at $0.5R$ and $\lambda=4.1$. Bottom right: cylindrical slice at $0.8R$ and $\lambda=4.1$.

The averaged and maximum y^+ at the blade SS obtained with grid FHR for all considered TSRs are reported in Fig. 18, highlighting again that this parameter is of order 1.

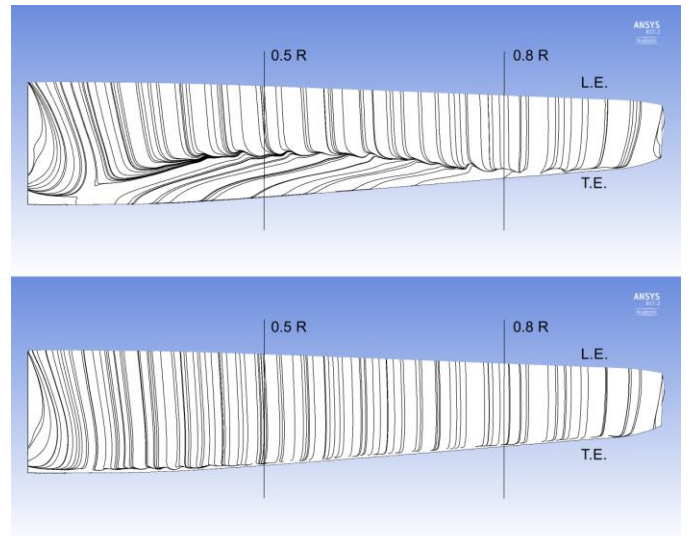


Fig. 17. Computed wall shear stress lines on the SS of the blade of the towing tank TCT at $\omega=96$ RPM and $Re_c=8.4$ million. Top: wall shear stress lines at $\lambda=2.81$. Bottom: wall shear stress lines at $\lambda=4.1$.

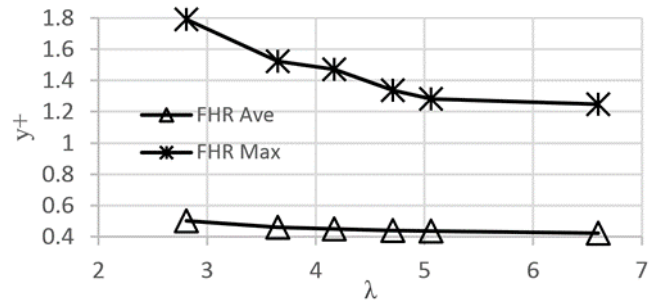


Fig. 18. Minimum and averaged y^+ on the SS of the blade of the towing tank TCT against TSR at $\omega=96$ RPM and $Re_c=8.4$ million.

B. Unsteady Analyses

The effects of typical differences between the Reynolds number of towing tank tests and field installations are considered in this section. The operating parameters common to the two cases are $U=0.89$ m/s, $\lambda=4.1$, current number $\mu=0.2$, and oscillatory frequency f of the secondary carriage of 0.5 Hz. As in the steady analyses above, the two cases differ only for Re_c at $0.75R$, which is about 70 times larger for the field TCT. The C_{My} loops determined by the fully turbulent CFD simulations using grid CLR for the $Re_c=116,000$ case and grid FHR for the high Reynolds number case are plotted against the instantaneous TSR in Fig. 19. One sees that the instantaneous moment levels are about 20 percent higher at high Reynolds number, although the amplitude of the moment cycles are comparable at both Reynolds numbers. Moreover, for the considered frequency, there is practically no hysteric effect at $Re_c=8.4$ million, indicating extremely small inertia component.

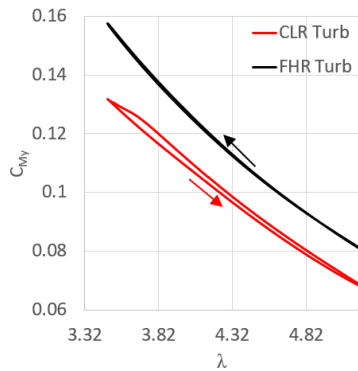


Fig. 19. Comparison of CFD results for the time-dependent low- and high--Reynolds number out-of-plane blade root bending moment against instantaneous TSR at $\omega=96$ RPM, mean $\lambda=4.1$, $\mu=0.2$ and $f=0.5$ Hz. ('CLR': coarse grid for $Re_c=116,000$ analysis; 'FHR': fine grid for $Re_c=8.4$ million analysis; 'Turb': fully turbulent simulation).

VI. CONCLUSIONS

The paper presented initial results of the NS CFD analysis of a towing tank TCT experiment in which steady power, force and moment coefficients, and unsteady moment coefficients due to oscillatory planar motion of the turbine were measured. For the steady regimes, the overall agreement of measured data and computed results at low and optimal TSR is fairly good, whereas CFD overpredicts power and loads as TSR increases from the optimal to the considered maximum values. Based on published data and theoretical analyses, this occurrence is unlikely to be due to the lack of blockage and free surface modelling in the presented simulations, but this aspect is being further investigated. CFD results also show that a fairly modest increment of 30 percent of the Reynolds number Re_c based on chord length and blade speed at 75 percent of the rotor radius (from 88,000 to 116,000) significantly reduces stall over all considered TSRs. For the unsteady regimes, CFD predicts the amplitude of the out-of-plane blade root bending moment fairly well, although predicted load cycles have lower means and less hysteresis than measured cycles. It is also found that the use of transition modelling yields improved predictions of unsteady loads at low Re_c , but has little impact at higher Re_c .

The paper also provided a first CFD-based quantitative assessment of the sensitivity of turbine performance and blade loads to blade Reynolds number variations from the low values typical of towing and flume tank tests (about 100,000) to the high values of field installations (about 8 million). It was found that both steady and unsteady performance and load parameters at field scale are about 20 percent higher than at tank scale due to thinner fully turbulent boundary layers more resilient to adverse pressure gradient in the former case. This conclusion is not unexpected for the relatively simple operating conditions considered, but this validation step is essential for future use of CFD to reliably analyse more complex TCT flows, like those due to misalignments of wave and tidal stream directions. These conditions may yield significant dynamic stall and unsteady loads also at field installation Reynolds number; their analysis with engineering codes will need new high-fidelity data to further improve modelling capabilities of these codes.

ACKNOWLEDGMENTS

All CFD simulations were performed on the HEC cluster of Lancaster University, which is kindly acknowledged.

REFERENCES

- [1] Crown Estate, *UK Wave and Tidal Key Resource Areas Project*, 2012. [Online] Available: <http://www.thecrownestate.co.uk/media/5476/uk-wave-and-tidal-key-resource-areas-project.pdf>, (accessed: 15/03/2017).
- [2] F. Maganga, G. Germain, J. King, G. Pinon, E. Rivoalan, *Experimental characterisation of flow effects on marine current turbine behaviour and on its wake properties*, IET Renew. Power Gen., 4(6): 498–509, 2010.
- [3] P.W. Galloway, L.E. Myers, A.S. Bahaj, *Studies of a scale tidal turbine in close proximity to waves*, 3rd Int. Conf. Ocean Energy, Bilbao, 2010.
- [4] E.E. Lust, L. Luznik, K.A. Flack, J.M. Walker, M.C. Van Benthem, *The influence of surface gravity waves on marine current turbine performance*, Int. J. Marine Energy, Vol. 3-4, pp. 27-40, 2013.
- [5] N. Barltrop, K.S. Varyani, A. Grant, X.P. Pam, *Investigation into wave-current interactions in marine current turbines*, Proceeding of ImechE, Part A: Journal of Power and Energy, Vol. 221, no. 2, 2007.
- [6] I.A. Milne, A.H. Day, R.N. Sharma, R.G.J. Flay, *The characterisation of the hydrodynamic loads on tidal turbines due to turbulence*, Renewable and Sustainable Energy Reviews, Vol. 56, pp. 851-864, 2016.
- [7] I.A. Milne, A.H. Day, R.N. Sharma, R.G.J. Flay, *Blade loads on tidal turbines in planar oscillatory flow*, Ocean Eng., 60: 163-174, 2013.
- [8] S.C. Tedds, I. Owen, R.J. Poole, *Near-wake characteristics of a model horizontal axis tidal stream turbine*, Renewable Energy, Vol. 63, pp. 222-235, 2014.
- [9] P. Mycek, B. Gaurier, G. Germain, G. Pinon, E. Rivoalan, *Experimental study of the turbulence intensity effects on marine current turbines behaviour. Part II: Two interacting turbines*, Renewable Energy, Vol. 68, pp. 876-892, 2014.
- [10] T. Stallard, B. Collings, T.Feng, J. Whelan, *Interactions between tidal turbine wakes: experimental Study of a group of three-bladed rotors*, Philosophical Transactions of the Royal Society A, 371: 20120159, 2013.
- [11] A. S. Bahaj, L. E. Myers, R. I. Rawlinson-Smith and M. Thomson, *The Effect of Boundary Proximity Upon the Wake Structure of Horizontal Axis Marine Current Turbines*, J. Offshore Mech. Arct., 134(2), 2012.
- [12] M.S. Campobasso, A. Piskopakis, J. Drofelnik, A. Jackson, *Turbulent Navier-Stokes Analysis of an Oscillating Wing in a Power Extraction Regime Using the Shear Stress Transport Turbulence Model*, Computers and Fluids, Vol. 88, pp. 136-155, 2013.
- [13] I. Afgan, J. McNaughton, S. Rolfo, D.D. Apsley, T. Stallard, P. Stansby, *Turbulent flow and loading on a tidal stream turbine by LES and RANS*, International Journal of Heat and Fluid Flow, Vol. 43, pp. 96-108, 2013.
- [14] S.C. Tatum, C.H. Frost, M. Allmark, D.M. O'Doherty, A. Mason-Jones, P.W. Prickett, R.I. Grosvenor, C.B. Byrne, T. O'Doherty, *Wave-current interaction effects on tidal stream turbine performance and loading characteristics*, Int. J. Marine Energy, Vol. 14, pp. 161-179, 2016.
- [15] D.M. Somers, *The S814 and S815 Airfoils*, Technical Report, NREL/SR-500-36292, 2014.
- [16] V. Casulli, *A semi-implicit finite difference method for non-hydrostatic, free-surface flows*, Int. J. Numer. Meth. Fl., 30(4): 425-440, 1999.
- [17] F.R. Menter, *Two-Equation Eddy-Viscosity Turbulence Models for Engineering Applications*, AIAA J., Vol. 32, no. 8, pp. 1598-1695, 1994.
- [18] D.C. Wilcox, *Simulation of Transition with a Two-Equation Turbulence Model*, AIAA J., Vol. 32, no. 2, pp. 247-255, 1994.
- [19] F. R. Menter, P.E. Smirnov, T. Liu, R. Avancha, *A One-Equation Local Correlation-Based Transition Model*, Flow, Turbulence and Combustion, Vol. 95, no. 4, pp. 95: 583, 2015.
- [20] G. Currie, N. Osbourne, D. Groulx, *Numerical Modelling of a Three-Bladed NREL S814 Tidal Turbine*, AWTEC, Singapore, 2016.
- [21] A.S. Bahaj, A.F. Molland, J.R. Chaplin, W.M.J. Batten, *Power and thrust measurements of marine current turbines under various hydrodynamic flow conditions in a cavitation tunnel and a towing tank*, Renewable Energy, Vol. 32, pp. 407-426, 2007.
- [22] J.I. Whelan, J.M.R. Graham, J. Peiro, *A free-surface and blockage correction for tidal turbines*, J. Fluid Mech., Vol. 624, pp. 281-291, 2009.
- [23] J.I. Whelan, T. Stallard, *Arguments for modifying the geometry of a scale model rotor*, EWTEC, Southampton, 2011.